

DESIGN OF MEASUREMENT SETUP FOR HIGH-ALTITUDE IN-FLIGHT EXPERIMENTS ON DU89-134/14 AIRFOIL AT LOW REYNOLDS NUMBER

Matija Avirović^{1,2,3}, Carlo Brunelli^{1,3,4}, Kevin Wykes⁵, Carl Mengdehl⁵, Benoît G. Marinus¹, Joris Degroote^{2,6} & Jeroen van Beeck³

¹Royal Military Academy, Brussels, Belgium

²Ghent University, Ghent, Belgium

³Von Karman Institute for Fluid Dynamics, Sint-Genesius-Rode, Belgium

⁴Vrije Universiteit Brussel, Brussels, Belgium

⁵Stemme Belgium, Namur, Belgium

⁶Flanders Make, Ghent, Belgium

Abstract

Two measurement setup configurations for high-altitude in-flight experiments are evaluated, with the configuration where the test airfoil is mounted vertically under the test aircraft wing showing clear advantages. The test airfoil design as well as the design of systems architecture based on the aforementioned configuration is presented. The steady 3D RANS numerical simulations with the transitional $(\gamma - Re_{\theta})$ SST turbulence model have been used to examine the effects of the test aircraft on the flow field around the test airfoil. Based on the analysis of the pressure and skin friction coefficient distributions it can be concluded that the flow field around the test airfoil is uniform between between s/c = 0.29 to s/c = 0.71.

Keywords: HAPS, UAV, In-Flight Experiments, Infrared Thermography, Temperature Sensitive Paint

1. Introduction

High-Altitude Pseudo-Satellites or High-Altitude Platform Systems (HAPS), are Unmanned Aerial Vehicles (UAVs) designed to operate within the lower layer of the stratosphere at altitudes between 15 and 20 km. Compared to traditional satellite systems, HAPS have lower operational costs, are simple to deploy, and have the potential to provide local aerial coverage for prolonged periods of time. Due to very limited energy storage capacity onboard HAPS, they have to rely on solar panels to charge batteries to power the propulsion and other onboard systems. Therefore accurately predicting the flow behaviour at high altitudes and designing airfoils with superior aerodynamic efficiency would allow for longer deployment times or greater payload carrying capacity [1, 2, 3].

Operating at high altitudes and at low speeds poses numerous challenges, particularly in terms of the flow around HAPS wings. In such operational conditions, the flow is characterized by low temperature $T\approx 217\,\mathrm{K}$, low Mach number $Ma\approx 0.1-0.2$, and low chord-based Reynolds number $Re_c\leq 5\times 10^5$. It is known that airfoil performance deteriorates in the low Reynolds number regime, mainly due to the frequent occurrence of Laminar Separation Bubbles (LSB), which leads to a decrease in lift and an increase in drag [4, 5, 6, 7, 8, 9]. Moreover, in such conditions flow separation, transition, and formation of the LSB are all very sensitive to changes in Reynolds number, pressure gradient, and external perturbations. Because of the important role of separation and transition on boundary layer development, their small changes can have a significant effect on the overall performance of the airfoil [4, 10, 11].

Given the complex nature of the flow around the HAPS wings, performing in-flight experiments under HAPS operating conditions has the potential to bring new insights into the flow phenomena and bridge the gap between ground testing experiments and numerical simulations. However, the successful

execution of in-flight experiments requires meticulous planning from the early design stages to avoid unnecessary expenses and ensure the safe execution of experimental measurements.

2. Objectives and overview of experimental configurations

The goal of this work is to design a measurement setup for high-altitude in-flight experiments and to investigate the aerodynamic impact of the in-flight experimental configuration on the test aircraft and test airfoil. The in-flight experimental measurements will be performed on the DU89-134/14 airfoil [12] due to its close geometrical similarity with an airfoil used in a HAPS flight demonstrator currently under development. The HAPS flight demonstrator depicted in Figure 1 is an evolution of an existing sailplane which retains its original wing design and will be used as an unmanned test aircraft platform for the experimental measurements.



Figure 1 – HAPS flight demonstrator H001 by Stemme Belgium under development

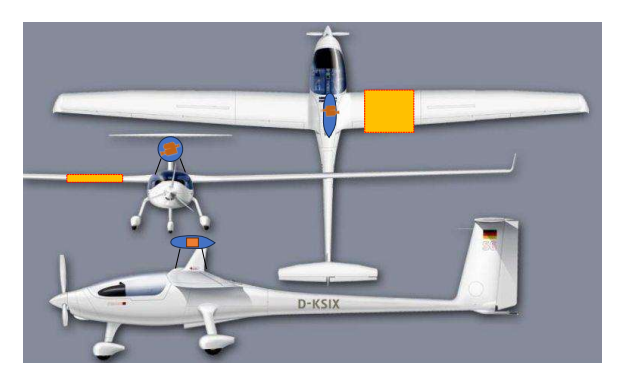
To gather knowledge about the flow properties around the DU89-134 airfoil in the operational conditions of HAPS, several experimental methods that have been proven in in-flight experiments will be employed. Pressure measurements are common in various in-flight experiments [13, 14, 15, 16] and will be used to the determine pressure distributions around the test airfoil, while the Infrared Thermography (IRT) [17, 18] and Temperature Sensitive Paint (TSP) [19, 20] experimental methods will be used to study the laminar-turbulent transition over the suction side of the test airfoil.

With the stated experimental objectives in mind, it is necessary to determine the location of the test airfoil which will allow for the installation of the pressure sensors and the location of the infrared and high-speed cameras which will allow for a good Field Of View (FOV) for IRT and TSP experiments. Common approaches to in-flight experiments include mounting the test airfoil vertically under the existing test aircraft wing and observing the test airfoil with a camera mounted in the cockpit or fuselage of the high-wing test aircraft [21, 22]. This configuration of the HAPS demonstrator with the test airfoil is illustrated in Fig 2a. The main advantages of this approach are that it offers plenty of space for test airfoil instrumentation, has small aerodynamic and structural impact, and is relatively easy to manufacture. Moreover, existing hardpoints can be used for mounting. Space for instrumentation is available within the airfoil as well as in the main wing immediately above the existing hard point openings. On the other hand, the flow quality can be affected due to the small aspect ratio of the test airfoil and the proximity of the test aircraft wing. In this case, the aspect ratio is limited by the ground clearance safety margin to ensure safe take-off and landing, therefore the maximal possible span of the test airfoil is $0.7\,\mathrm{m}$. To mitigate the the effects of a small aspect ratio and wing tip recirculation the end plate that extends $25\,\mathrm{mm}$ will be added to the test airfoil.

Another common approach is to mount the test airfoil around the existing test aircraft wing in a so-called "wing glove" and then place the cameras either in the fuselage/cockpit for low-wing aircraft [18, 17, 23, 13] or on a pylon above the fuselage/cockpit for high-wing aircraft [24]. This configuration is depicted in Fig. 2b, similarly to the previous case this configuration has a small aerodynamic and structural impact. However, when compared to the previous configuration, it offers less space for test airfoil instrumentation, as sensors and cabling cannot be installed inside the airfoil due to the



(a) Configuration 1 - Test airfoil mounted vertically under the test aircraft wing, IR and high-speed cameras are placed in cockpit



(b) Configuration 2 - Test airfoil mounted over the test aircraft wing, IR and high-speed cameras are placed in a pod on a pylon above fuselage

Figure 2 – Different configurations for mounting the test airfoil and positioning the infrared and high-speed cameras on the test aircraft. NB: The images are not an accurate representation of the test aircraft, test airfoil or camera positions and are used only for illustrative purposes

thin shell around the existing wing, making integration challenging without tampering with the existing wing skin. Furthermore, there is a high risk of camera pod flutter because it is placed on a pylon above the fuselage/cockpit.

A comparative overview between the two configurations is given in Table 1. Although Configuration 2 in theory offers better flow quality over the test airfoil it also introduces a high risk of flutter and increases manufacturing complexity, therefore after careful evaluation, it was decided to proceed towards the in-flight tests with Configuration 1.

Test airfoil configuration	Configuration 1	Configuration 2
Aerodynamic impact of test airfoil	Small	Small
Structural impact of test airfoil	Small	Small
Flutter impact of test airfoil	Medium	Small
Flutter impact of camera pod	None	High
Flow quality over test airfoil	Good	Excellent
Camera integration difficulty	Medium	High
Test airfoil instrumentation	Enough space	Space constrained
Manufacturing difficulty	Medium	High

Table 1 – Comparative assessments of different in-flight experimental configurations, green=advantage, yellow=neutral, red=disadvantage

3. Design of measurement setup

3.1 Test airfoil

The DU89-134/14 test airfoil is going to be manufactured out of basalt composite wrapped around the foam core and is going to be attached vertically under the test aircraft wing (Fig. 2a) on the existing hardpoints. This particular location has been chosen because it allows a good field of view (FOV) for the infrared and optical high-speed cameras and has a minimal aerodynamic and structural impact on the test aircraft. The angle of attack adjustment is going to be made via the attachment plate between the test airfoil and the test aircraft wing displayed in Fig. 3a. This setup will allow adjustment of the angle of attack from $\alpha=-1^\circ$ to $\alpha=7^\circ$ in one-degree increments by rotating the attachment plate and securing it with bolts to the corresponding holes. To allow the installation of pressure sensors and other necessary equipment the access door has been foreseen on the pressure side of the airfoil as depicted in Fig. 3c.

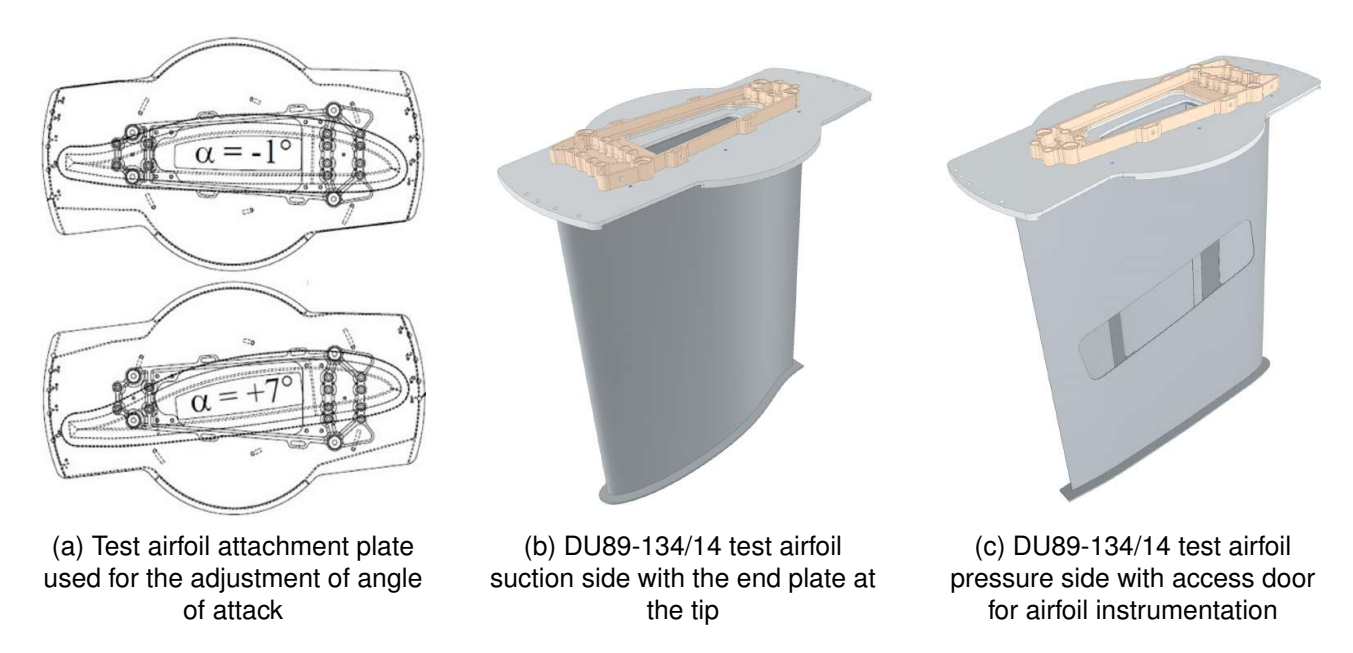


Figure 3 – Concept overview of the test airfoil assembly

3.2 Systems architecture

The measurement setup systems architecture schematic is displayed in Figure 4. Given that the test aircraft is unmanned at those altitudes, the data acquisition (DAQ) is started with the trigger signal from the ground control or after a specified time delay. Once the trigger signal is received, the DAQ device (NI cRIO-9055) starts recording images from the Phantom VEO-E 340L high-speed and FLIR A655sc infrared cameras as well as amplified voltage signals from Taipro differential pressure sensors and Bosch BMP 280 absolute pressure sensors. The cryo-TSP that will be provided by the German Aerospace Center (DLR) is excited with UV LED light which is powered continuously. Since the cryo-TSP and IRT experimental methods require a difference in temperature between the test airfoil and the flow to detect laminar-turbulent transition, the test airfoil is equipped with a resistive electrical heating system.

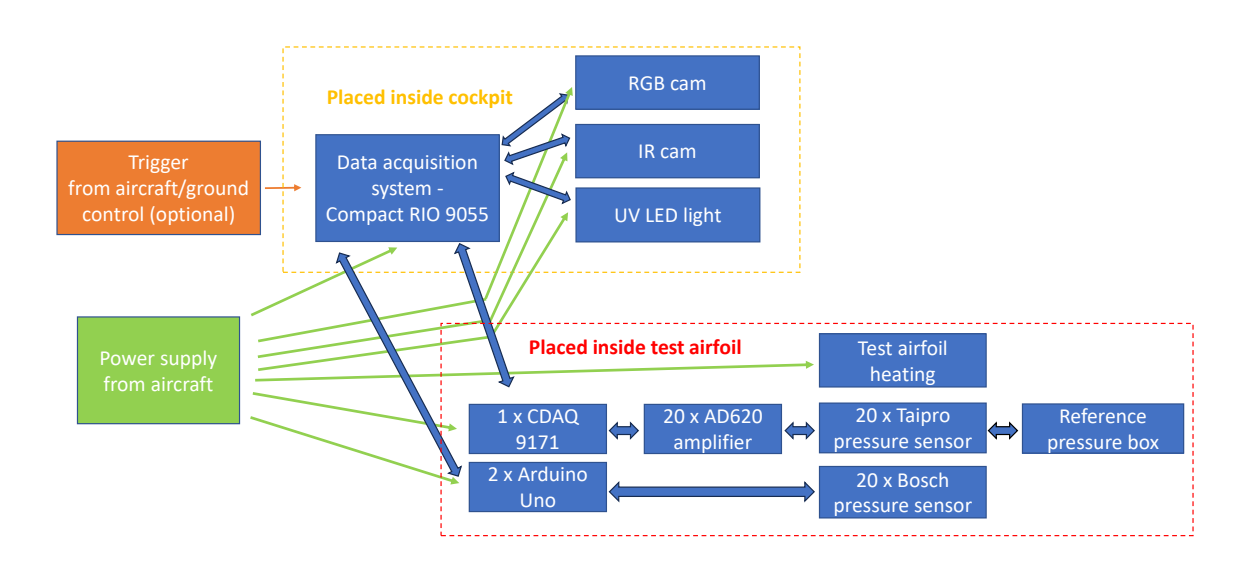


Figure 4 – Systems architecture schematic

3.3 IR camera field of view

The field of view of the IR camera was evaluated by building a true-to-scale replica of the test airfoil with the camera placed in the same position with respect to the test airfoil as in in-flight tests. Fig. 5 shows the FOV of the IR camera with lenses of different focal lengths f. As it can be seen from Fig. 5c IR camera equipped with the lenses of $f = 41.3 \, \mathrm{mm}$ captures the biggest section of the test airfoil chord and is, therefore, the preferred lens choice for the in-flight experiments. Since the FOV of the IR camera is skewed fiducial location markers similar to [25] will be used to dewarp the IR images. The red band depicted in Fig. 5 corresponds to the heated part of the test airfoil replica and is not representative of the final design.

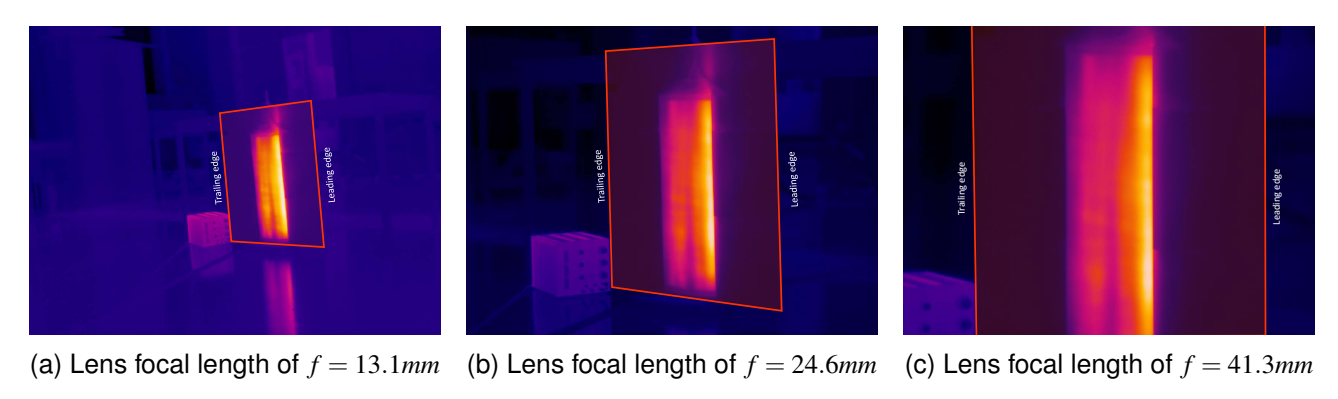


Figure 5 – IR camera FOV assessment using different focal length lenses

4. Numerical simulations

4.1 Spatial domain, discretization and boundary conditions

The spatial domain depicted in Fig. 6 is 75 test airfoil chord lengths long, 50 high and 25 wide, with the test aircraft placed at 25 test airfoil chord lengths from the inlet, top, bottom and side wall. The DU89-134/14 test airfoil is positioned in the exact same location on the test aircraft as it will be during in-flight experiments and is set at an angle of attack (AoA) of $\alpha = 5^{\circ}$ relative to the free-stream flow. The chord length of the DU89-134/14 test airfoil is $c = 0.6\,\mathrm{m}$ and the span corresponds to $s = 0.7\,\mathrm{m}$. A refinement region is applied around the test airfoil with the length of 16.6 chords and width and height of 3.3 chords.

To reduce the computational cost, a symmetry plane was placed through the mid-plane of the test aircraft. Furthermore, the test aircraft propeller with a diameter of $2\,\mathrm{m}$ was replaced with an actuator disk to match thrust. The swirl caused by the propeller is neglected. Slip-wall boundary conditions were assigned to the outer walls of the computational domain, no-slip wall boundary conditions to the test aircraft and DU89-134/14 test airfoil and finally velocity inlet and pressure outlet were assigned to the corresponding planes.

Spatial domain discretization was performed with ANSYS Fluent Meshing version 2023R2 using polyhexacore mesh. The DU89-134/14 test airfoil was discretized with the surface mesh cell size of $2\,\mathrm{mm}$ and 30 inflation layers with a first layer height of $0.025\,\mathrm{mm}$ and growth rate of 1.1 to ensure that the wall y^+ values remain below 1. The rest of the test aircraft was discretized using a surface mesh cell size of $20\,\mathrm{mm}$ and 20 inflation layers with a first layer height of $0.25\,\mathrm{mm}$ and growth rate of 1.2. Lastly, the refinement region around the test airfoil was discretized using a volume mesh size of $50\,\mathrm{mm}$. The final mesh consisted of 15.63×10^6 cells and 33.62×10^6 computational nodes.

4.2 Numerical model

The steady 3D RANS simulations of the flow around the test aircraft and DU89-134/14 test airfoil are performed with the transitional $(\gamma - Re_{\theta})$ SST turbulence model integrated within the commercial software ANSYS Fluent version 2023R2. The transitional SST model couples the shear-stress transport model $(k - \omega$ SST) developed by Menter [26] with the transport equations for the intermittency γ and transition momentum thickness Reynolds number Re_{θ} [27, 28]. This particular turbulence model

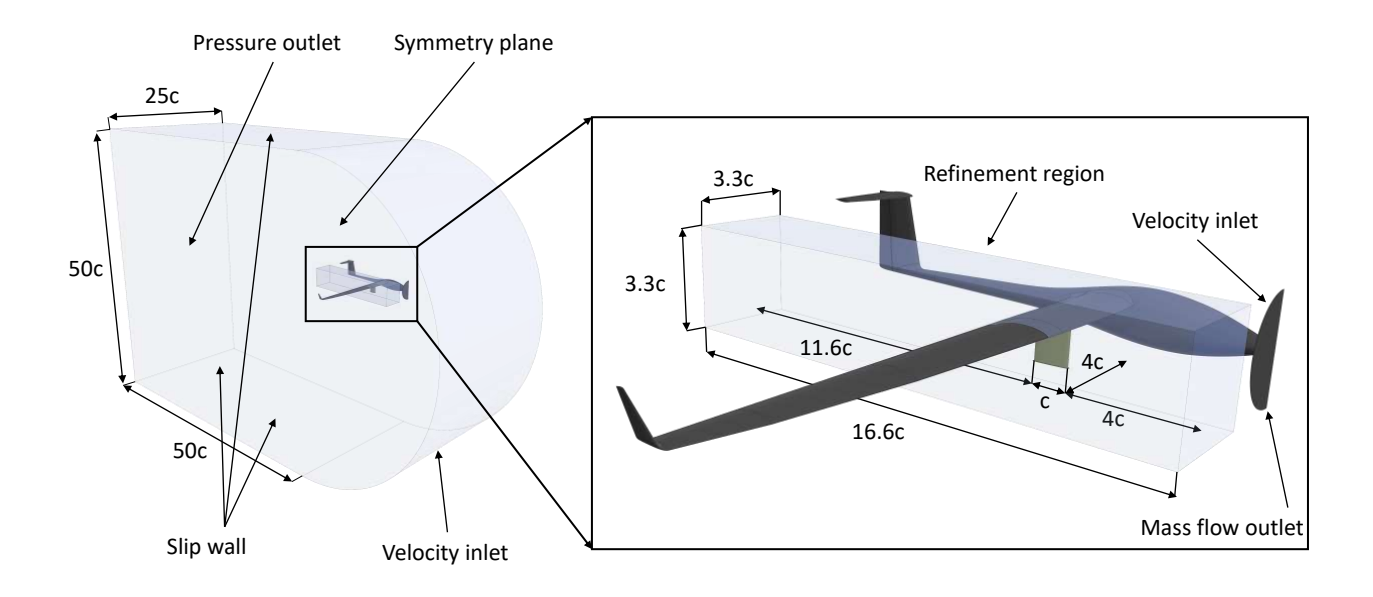


Figure 6 – Spatial domain dimensions with boundary conditions and refinement region around the DU89-134/14 test airfoil

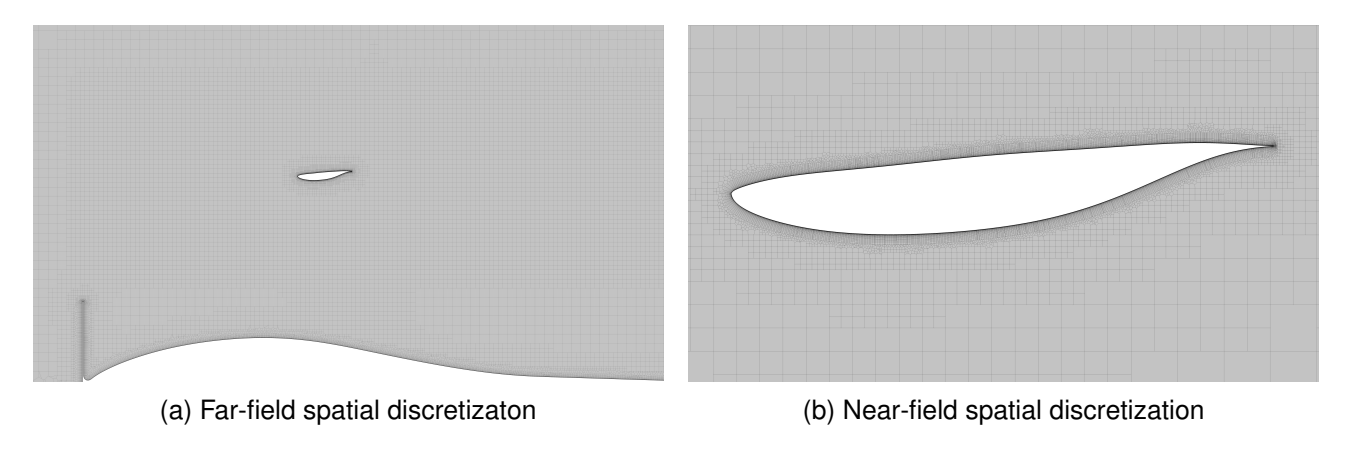


Figure 7 – Spatial domain discretization for the test airfoil at a spanwise location of s/c = 0.43

has been chosen because of its good accuracy in predicting flow separation in low Reynolds number flows and acceptable computational cost [29].

4.3 Computational settings

Pressure—velocity coupling is performed with the Coupled algorithm. The Green—Gauss node scheme is used for the gradient evaluation while second-order interpolation is used for the pressure equation and second-order upwind discretization schemes are used for the convective terms.

The free-stream inlet velocity, air density, and air dynamic viscosity are chosen to correspond to the DU89-134/14 test airfoil chord-based Reynolds number of $Re_c = 5 \times 10^5$ at $16 \, \mathrm{km}$ of altitude. Parameters used for modelling the propeller, like disk inlet velocity magnitude and mass flow outlet rate were based on the thrust coefficient and rotational speed of the propeller in similar flow conditions according to [30].

5. Results

Pressure and skin friction coefficient distributions over the test airfoil pressure and suction sides under an angle of attack of $\alpha = 5^{\circ}$ are depicted in Fig. 9. They are assessed for different spanwise locations

depicted in Fig. 8 along the test airfoil to observe if there is a significant flow nonuniformity between the root and the tip of the airfoil.

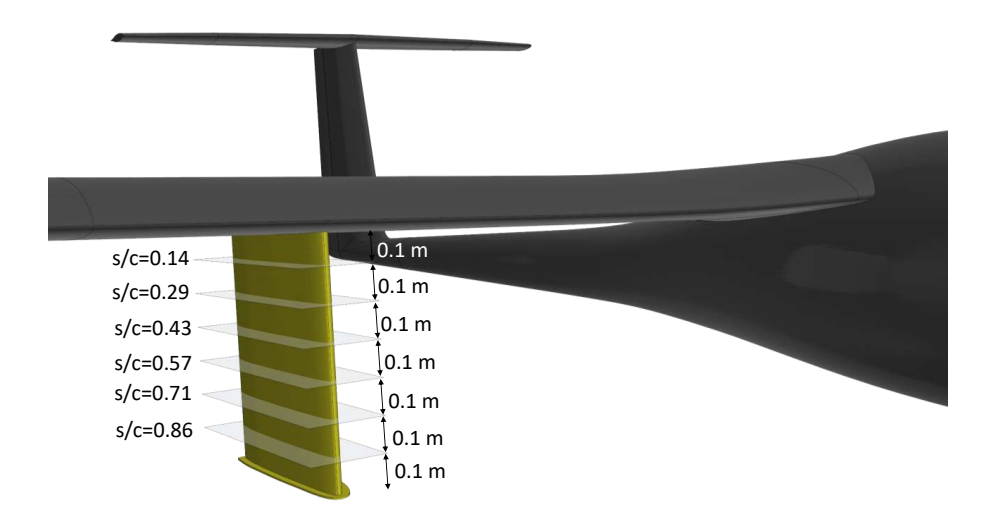


Figure 8 – Close-up view of the inspection planes along the span of the DU89-134/14 test airfoil used to compare pressure and skin friction coefficients in Fig 9

From the pressure coefficient distributions in Fig. 9a, it can be seen that for the pressure side of the test airfoil, they show very similar behaviour over the chord and along the span. On the other hand, by observing the pressure coefficient distributions over the suction side it can be concluded that the flow field is fairly uniform between s/c=0.29 to s/c=0.71, while for s/c=0.14 and s/c=0.86, it can be noted that the pressure coefficient distributions show different values. The same flow features can be spotted by observing the skin friction coefficient distributions in Fig. 9b. Over the pressure side of the test airfoil, the skin friction coefficient values show almost identical behaviour while over the suction side, only the values for s/c=0.14 and s/c=0.86 significantly differ from other spanwise locations. This behaviour can be explained by taking a closer look at the velocity magnitude contours displayed in Fig. 11a and Fig. 11b where it can be seen that over the suction side of the test airfoil, there is a spanwise decrease of velocity magnitude from the root of the airfoil towards the airfoil tip. This explains the higher suction peak in the pressure coefficient distribution for s/c=0.14 and the gradual decrease in suction towards s/c=0.86.

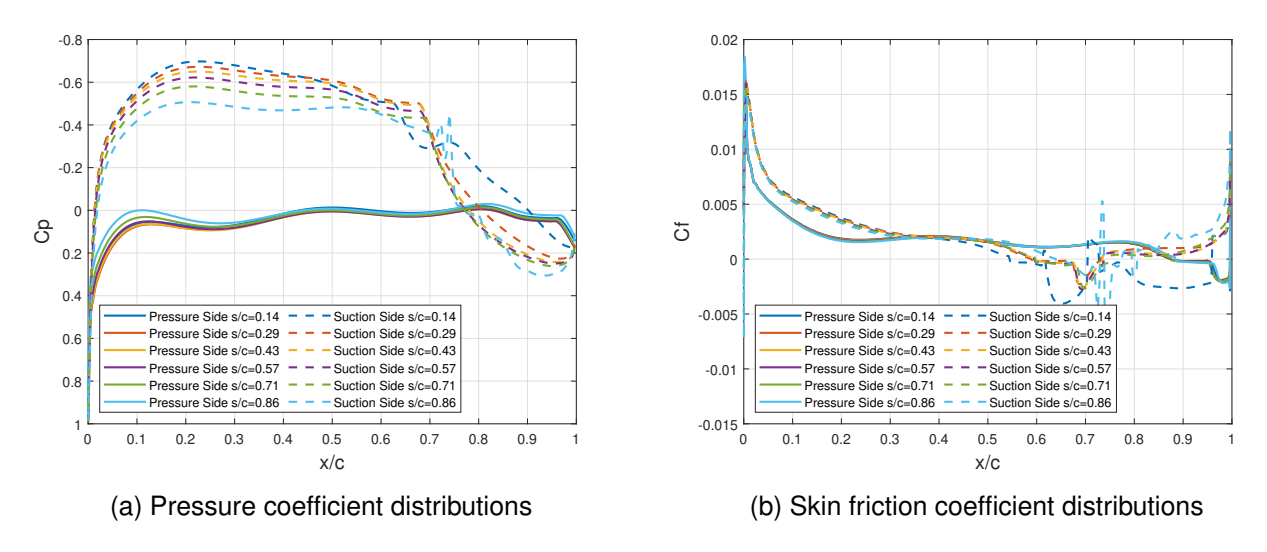


Figure 9 – Pressure and skin friction coefficient distributions for different spanwise inspection planes from Fig. 8

Velocity magnitude contours illustrated in Fig. 10 and in Fig.11 exhibit that the propeller wake has a negligible effect on the flow around the test airfoil. Conversely by carefully observing the flow field

in Fig. 10a,10b and 10c it can be seen that the test airfoil is located in an area of lower velocity magnitude compared to the freestream velocity magnitude, which is caused by the test aircraft airfoil located just above the test airfoil.

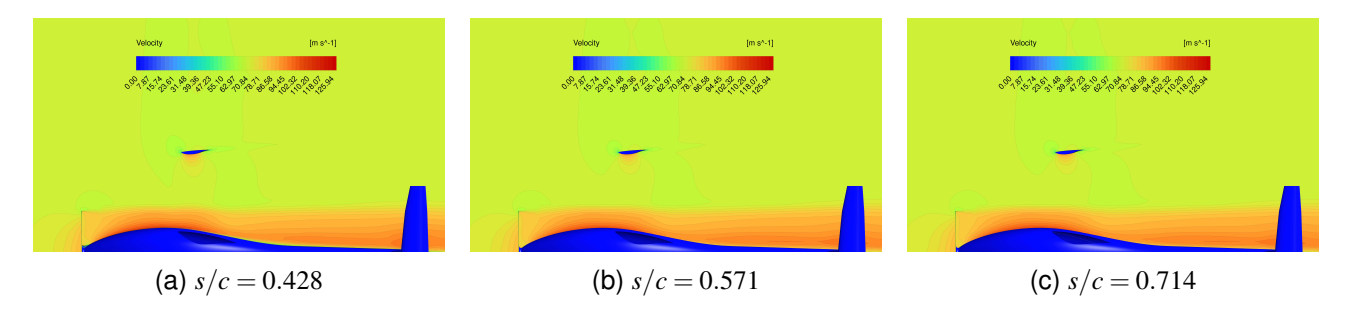


Figure 10 – Velocity magnitude contours for different spanwise locations along DU89-143/14 test airfoil

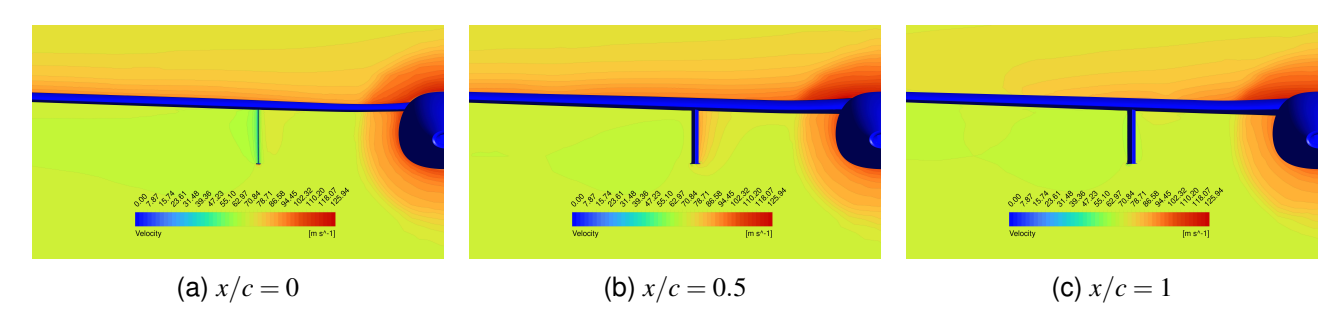


Figure 11 – Velocity magnitude contours for different chordwise locations along DU89-143/14 test airfoil

6. Conclusions

Based on the presented results it can be concluded that the measurement setup for high-altitude in-flight experiments with the test airfoil mounted vertically under the test aircraft wing has a minor aerodynamic impact on the test aircraft. Simultaneously this configuration allows for good field of view for infrared and high-speed cameras, as well as plenty of space for test airfoil instrumentation. The 3D RANS numerical simulations showed that the flow quality over the mid-span section of the test airfoil is satisfactory and is not greatly affected by the test aircraft and therefore allows performing in-flight experimental measurements.

7. Acknowledgments

The authors would like to acknowledge Christian Klein from the German Aerospace Center (DLR) for providing us with the cryo-TSP-coated airfoil samples for wind tunnel testing.

8. Contact Author Email Address

Contact the authors at: matija.avirovic@mil.be and carlo.brunelli@mil.be

9. Copyright Statement

The authors confirm that they, and/or their company or organization, hold copyright on all of the original material included in this paper. The authors also confirm that they have obtained permission, from the copyright holder of any third-party material included in this paper, to publish it as part of their paper. The authors confirm that they give permission, or have obtained permission from the copyright holder of this paper, for the publication and distribution of this paper as part of the ICAS proceedings or as individual off-prints from the proceedings.

References

- [1] Flavio Araripe D'Oliveira, Francisco Cristovão Lourenço De Melo, and Tessaleno Campos Devezas. Highaltitude platforms Present situation and technology trends. *Journal of Aerospace Technology and Management*, 8:249–262, 2016.
- [2] G. Romeo, G. Frulla, and E. Cestino. Design of a high-altitude long-endurance solar-powered unmanned air vehicle for multi-payload and operations. *Proceedings of the Institution of Mechanical Engineers, Part G: Journal of Aerospace Engineering*, 221:199–216, 2007.
- [3] Jesús Gonzalo, Deibi López, Diego Domínguez, Adrián García, and Alberto Escapa. On the capabilities and limitations of high altitude pseudo-satellites. *Progress in Aerospace Sciences*, 98:37–56, 4 2018.
- [4] Michael S. Selig and James J. Guglielmo. High-Lift Low Reynolds Number Airfoil Design. *Journal of Aircraft*, 34(1):72–79, 1997.
- [5] Abhijit Mitra, P. Gokul, and O. N. Ramesh. The role of laminar separation bubble on low Reynolds number airfoils. 51st AIAA Aerospace Sciences Meeting including the New Horizons Forum and Aerospace Exposition, 2013.
- [6] Ashok Gopalarathnam, Benjamin A. Broughton, Bryan D. McGranahan, and Michael S. Selig. Design of low Reynolds number airfoils with trips. *Journal of Aircraft*, 40:768–775, 2003.
- [7] M. M. O'meara and T. J. Mueller. Laminar separation bubble characteristics on an airfoil at low Reynolds numbers. *AIAA Journal*, 25:1033–1041, 1987.
- [8] Edward J. Fitzgerald and Thomas J. Mueller. Measurements in a separation bubble on an airfoil using laser velocimetry. *AIAA Journal*, 28:584–592, 1990.
- [9] P. Lissaman. Low-Reynolds-Number Airfoils. *Annual Review of Fluid Mechanics*, 15:223–239, 11 2003.
- [10] S. Wang, Y. Zhou, Md Mahbub Alam, and H. Yang. Turbulent intensity and Reynolds number effects on an airfoil at low Reynolds numbers. *Physics of Fluids*, 26, 11 2014.
- [11] T.J. Mueller, L. J. Pohlen, P. E. Conigliaro, and B. J. Jansen. The influence of free-stream disturbances on low Reynolds number airfoil experiments. *Experiments in Fluids*, pages 3–14, 1983.
- [12] L.M.M Boermans and Arne van Garrel. Design and Windtunnel Test Results of a Flapped Laminar Flow Airfoil For High-Performance Sailplane Applications. *The International Council of the Aeronautical Sciences Congress*, 09 Anaheim, 1994.
- [13] Christian Raab and Kai Rohde-Brandenburger. In-Flight Testing of MEMS Pressure Sensors for Flight Loads Determination. *AIAA Scitech 2020 Forum*, 2020.
- [14] Sascha U. Kienitz, Laura Lohr, Markus J. Schmid, and Alexander W. Koch. Static and Dynamic Pressure Measurement in Flight Test Application With Optical Fabry–Pérot Sensors. *IEEE Transactions on Instrumentation and Measurement*, 70:1–11, 2021.
- [15] Long P. Yip, Paul M. H. W. Vijgen, Jay D. Hardin, and C. P. van Dam. In-flight Pressure Measurements on a Subsonic Transport High-Lift Wing Section. *Journal of Aircraft*, 32(3):529–538, 1995.
- [16] Gian-Andrea Heinrich, Stephanie Vogt, Nicholas R. J. Lawrance, Thomas J. Stastny, and Roland Y. Siegwart. In-Wing Pressure Measurements for Airspeed and Airflow Angle Estimation and High Angle-of-Attack Flight. *Journal of Guidance, Control, and Dynamics*, 45(6):1033–1045, 2022.
- [17] William S. Saric, David E. West, Matthew W. Tufts, and Helen L. Reed. Experiments on Discrete Roughness Element Technology for Swept-Wing Laminar Flow Control. *AIAA Journal*, 57(2):641–654, 2019.
- [18] Tihao Yang, Yifu Chen, Yayun Shi, Jun Hua, Feifei Qin, and Junqiang Bai. Stochastic Investigation on the Robustness of Laminar-Flow Wings for Flight Tests. *AIAA Journal*, pages 1–21, 1 2022.
- [19] Kazuyuki Nakakita, Shunsuke Koike, Mitsuru Kurita, and Kazuya Masui. Flight PSP Measurement Test Using Beechcraft 65. 50th AIAA Aerospace Sciences Meeting including the New Horizons Forum and Aerospace Exposition, 2012.
- [20] Yosuke Sugioka, Hitomi Sato, Kazuyuki Nakakita, Tsutomu Nakajima, Taku Nonomura, and Keisuke Asai. In-Flight Visualization of Shock Wave on a Jet Aircraft Wing Using Lifetime-Based Pressure-Sensitive Paint Technique. *AIAA Scitech 2019 Forum*, 2019.
- [21] Brian Crawford, Glen Duncan, David West, and William Saric. Laminar-Turbulent Boundary Layer Transition Imaging Using IR Thermography. *Optics and Photonics Journal*, 03:233–239, 01 2013.
- [22] G.T. Duncan, Brian Crawford, Matthew Tufts, William Saric, and Helen Reed. Flight Experiments on the Effects of Step Excrescences on Swept-Wing Transition. *International Journal of Engineering Systems Modelling and Simulation*, 6:171–180, 01 2014.
- [23] Aaron A. Tucker, William S. Saric, and Helen L. Reed. Laminar Flow Control Flight Experiment Design and Execution. *52nd Aerospace Sciences Meeting*, 2014.
- [24] K.-H. Horstmann, R. Mueller, C.-H. Rohardt, A. Quast, H. Echtle, W. Wohlrath, P. Dick, D. Welte, and

Design of Measurement Setup for High-Altitude In-Flight Experiments on DU89-134 Airfoil

- H.W. Stock. Design and Flight Test Evaluation of a Laminar Wing Glove on a Commuter Aircraft. 19th ICAS Congress, 1994, Anaheim, USA, Paper No.: ICAS-94-5.4.1, 1994.
- [25] Adrian Grille Guerra, Christoph Mertens, Jesse Little, and Bas van Oudheusden. Experimental characterization of an unsteady laminar separation bubble on a pitching wing. *Experiments in Fluids*, 64, 05 2023.
- [26] F. R. Menter. Two-equation eddy-viscosity turbulence models for engineering applications. *AIAA Journal*, 32:1598–1605, 1994.
- [27] F. R. Menter, R. B. Langtry, S. R. Likki, Y. B. Suzen, P. G. Huang, and S. Völker. A Correlation-Based Transition Model Using Local Variables: Part I Model Formulation. *Turbo Expo: Power for Land, Sea, and Air*, Volume 4: Turbo Expo 2004:57–67, 06 2004.
- [28] Robin Langtry and Florian Menter. Transition Modeling for General CFD Applications in Aeronautics. *43rd AIAA Aerospace Sciences Meeting and Exhibit*, 2005.
- [29] S. M.A. Aftab, A. S.Mohd Rafie, N. A. Razak, and K. A. Ahmad. Turbulence model selection for low Reynolds number flows. *PLoS ONE*, 11, 4 2016.
- [30] Benoit G. Marinus, Nikolaos Mourousias, and Ahmed Malim. Exploratory Optimizations of Propeller Blades for a High-Altitude Pseudo-Satellite. *AIAA AVIATION 2020 FORUM*, 2020.